A Dithering Algorithm for Local Composition Control with Three-Dimensional Printing

Wonjoon Cho **Emanuel M. Sachs** **Nicholas M. Patrikalakis** **Donald E. Troxel**

Massachusetts Institute of Technology
Cambridge, MA 02139-4307, USA

Design Laboratory Memorandum 2001-3

Copyright ©2002 Massachusetts Institute of Technology
All rights reserved

December 21, 2001
Revised: May 14, 2002

Abstract

A dithering algorithm is presented for application to Local Composition Control (LCC) with Three-Dimensional Printing (3D Printing) to convert continuous-tone representation of objects with LCC into discrete (point-wise) version of machine instructions. The algorithm presented effectively reduces undesirable low frequency textures of composition for individual three-dimensional layers and also for three-dimensional volumes. Peculiarities of the 3D Printing machine, including anisotropic geometry of its picture elements (PELs) and uncertainties in droplet placement, are addressed by adapting a standard digital halftoning algorithm. Without loss of generality, our algorithm also accounts for technical limitations in the printing device, only generating lattices that can be represented within the finite memory limits of the hardware.

Keywords : Solid Freeform Fabrication; 3D Printing; Local Composition Control; digital halftoning; dispersed-dot ordered dither; low frequency textures; anisotropic PEL; minimum run-length; pattern memory.

1 Introduction

Solid Freeform Fabrication (**SFF**) technology such as Selective Laser Sintering (SLS) [1], Laminated Object Manufacturing (LOM) [2], Stereolithography (SLA) [3], Shape Deposition Manufacturing [4], Selective Area Laser Deposition (SALD) [5], and Three-Dimensional Printing (3D Printing) [6, 7, 8, 9, 10], builds parts by repeatedly adding minute primitives of material according to a computer model until the final object is created. One of the great potential benefits offered by SFF technology is the ability to create parts that have composition variation within them. Such *Local Composition Control* (**LCC**) [11, 12, 13, 14, 15, 16, 1, 4] has the potential to create new classes of components. Material composition can be tailored within a component to achieve local control of properties (e.g., index of refraction, electrical conductivity, formability, magnetic properties, corrosion resistance,

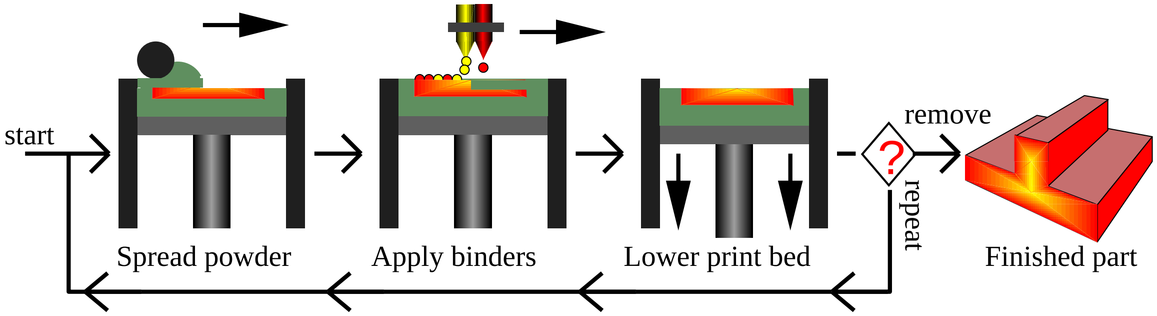

Figure 1: 3D Printing illustrating Local Composition Control (LCC)

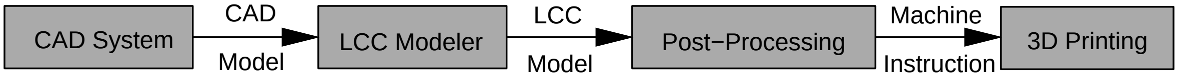

Figure 2: Information Pathway for LCC with 3D Printing

hardness vs. toughness, etc.). Alternatively, monolithic components can be created which integrate the function of multiple discrete components, saving part count, space and weight and enabling concepts that would be otherwise impractical. Controlling the spatial distribution of properties via composition variation will allow for control of the state of the entire component (e.g., the state of residual stress in a component). Integrated sensors and actuators can be envisioned which are enabled by LCC (e.g., bimetallic structures, in-situ thermocouples, etc.). Devices which have as their function the control of chemical reactions are possible. The utility of mesoscopic parts made by SFF will depend strongly on the ability to locally control the composition.

Among the SFF processes, *Three-Dimensional Printing* (**3D Printing**) is particularly well-suited to the fabrication of parts with LCC. 3D Printing creates parts in layers by spreading powder, and then ink-jet printing materials into the powderbed [6, 7, 8, 9, 10]. In some cases, these materials are temporary or fugitive glues, but in many cases, these materials remain in the final component. Examples of the latter include: ceramic particles in colloidal or slurry form, metallic particles in slurry form, dissolved salts which are reduced to metal in the powderbed, polymers in colloidal or dissolved form, and drugs in colloidal or dissolved form. 3D Printing has been extended to the fabrication of components with LCC by printing different materials in different locations, each through its own ink-jet nozzle(s). Figure 1 illustrates this conceptually with two different colors, each representing the printing of a different material into the powder bed with local control of position. 3D Printing is thus capable of fully three-dimensional control of composition on the scale of the binder droplets. SFF processes build parts directly from computer models. These models may originate from sampled volumetric data or solid models of parts designed within a CAD system. The processing of these models for fabrication is unique to each SFF system (depending on the architecture and mechanism of adding material) however, the general philosophy can be understood by looking at the information flow for 3D Printing, as shown in Figure 2.

Encouragement can be taken from the fact that in the 3D Printing research, several promising applications are under active development. Drug delivery devices are being created by printing different drugs at prescribed locations within the interior of a pill or implantable device. These drugs are then released into the body according to designed release profiles [17, 18]. A new program has begun on Gradient Index Lenses (**GRIN**) which refract light by gradients in the index of refraction, rather than by external geometry. Such lenses can provide the functionality normally associated

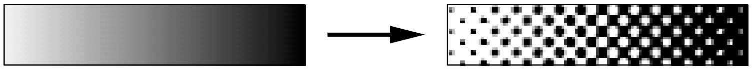

(a) clustered−dot ordered dither

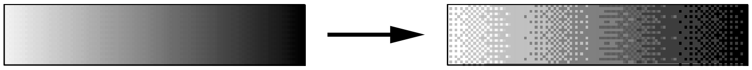

(b) dispersed−dot ordered dither

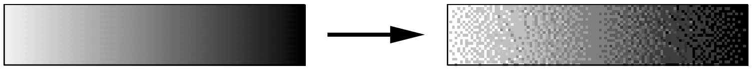

(c) error diffusion algorithm

Figure 3: Gray scale ramp: classical halftoning algorithms

with multi-component ground optics at lower cost and in a smaller space. The drug delivery and GRIN applications are for high value added devices which are small in size and thus can reasonably be manufactured by 3D Printing. LCC is also being applied to the fabrication of tooling by 3D Printing. Hard phases such as TiC are being printed local to the surface of a tool for increased wear resistance. Tools with local control of porosity (for venting of gasses) are being fabricated by printing a material which acts to block the infiltrant during furnace densification. Finally in a more recent application, scaffolds for tissue engineering are being developed.

Digital halftoning [19], often called spatial dithering, refers to any algorithmic process which creates the illusion of continuous-tone images from the judicious arranegement of binary picture elements. Since most hardcopy devices render images as binary or discrete tones, the halftoning technique is used to convert a continuous, ideal image within a computer representation into an appropriate form capable of being rendered on such devices. Since the 3D Printing machine is a binary device and builds objects in a point-wise fashion for each layer, in an analogous fashion to ink-jet printing on paper, a logical starting point for producing objects with LCC could be to extend the digital halftoning techniques. There exist various classical halftoning techniques, however most of them fall within one of the following categories: clustered-dot ordered dither; dispersed-dot ordered dither; and dynamic thresholding such as error diffusion algorithms – see also Figure 3. An ordered dither generates a bilevel representation of continuous-tone image by comparing the image intensity with a position-dependent pre-defined set of threshold values as illustrated in Figure 5. A clustered-dot ordered dither (Figure 3-(a)) mimics the photoengraving process used in printing, where tiny picture elements (PELs) collectively comprise dots of various sizes. If a display device can successfully accomodate an isolated PEL, then the preferred choice is a dispersed-dot ordered dither (Figure 3-(b)) which maximizes the use of resolution. In the error diffusion algorithm (Figure 3-(c)), instead of using the ordered set of threshold values, the error between an input image intensity and the displayed PEL intensity at a position is dispersed, or diffused to its neighboring PEL positions in such a way as to minimize the accumulated error between the input and displayed images. Overviews of those approaches can be found in literature, such as in Ulichney [19], Stoffel and Moreland [20], and Jarvis *et al.* [21].

Dispersed-dot ordered dither approach is particulary preferred for the application to 3D Printing because: “dispersed-dot” dither can avoid undesirable low frequency textures in the region of constant material composition; and “ordered” dither facilitates the control of the number of dither patterns represented within the limits of hardware’s pattern memories. Due to the three-dimensionality of

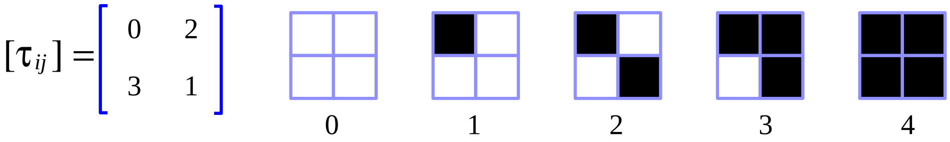

Figure 4: 2 × 2 dither array and its 5 patterns

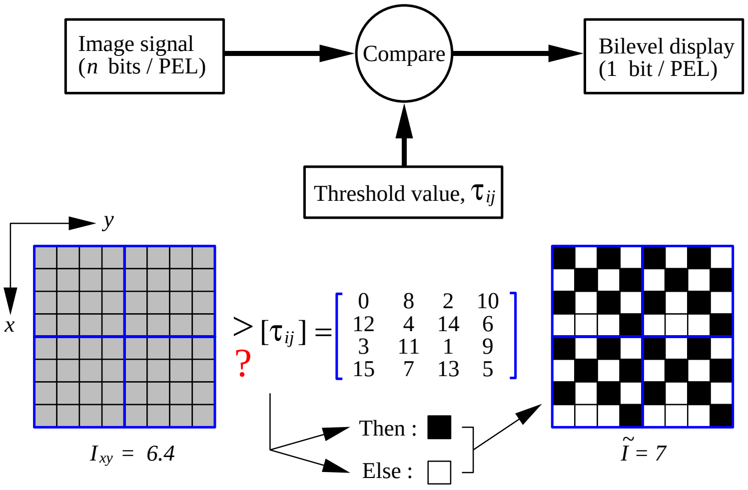

Figure 5: An ordered dithering process

the 3D Printing process, it will be necessary to create *volume* dithering patterns in order for successive layers not to be printed with the same pattern in the region of fairly uniform composition[1]. Furthermore, peculiarities of the 3D Printing device, including anisotropic geometry of its PELs and uncertainties in droplet placement, should be addressed.

This paper is structured as follow: section 2 formulates a dithering algorithm for LCC with 3D Printing; section 3 illustrates the proposed algorithm with a realistic example; and section 4 concludes the paper.

2 Generation of Dithering Algorithm

2.1 Review of Dispersed-Dot Ordered Dither

The ordered dither technique generates a bilevel representation of continuous-tone images by comparing the image intensities I_{xy} with a position-dependent set of threshold values τ_{ij}. The set of τ_{ij} is contained in $M \times N$ *dither array* with the choice of array element values and their arrangement in the array being the key to the dithering technique. The corresponding *dither pattern* specifies the order in which PELs are turned "on" in the lattice as the intensity increases, e.g., see Figure 4 for a 2×2 dither array and its 5 patterns. For an $M \times N$ dither array $[\tau_{ij}]$, ordered dithering is accomplished as follows. Each input intensity is scaled to the range $0 \leq I_{xy} \leq MN$. If I_{xy} is to be applied to image position (x, y), the corresponding row and column (i, j) for the dither array will

---

[1] Replicating layers of the same two-dimensional dither pattern will always create vertical streaks of the same material.

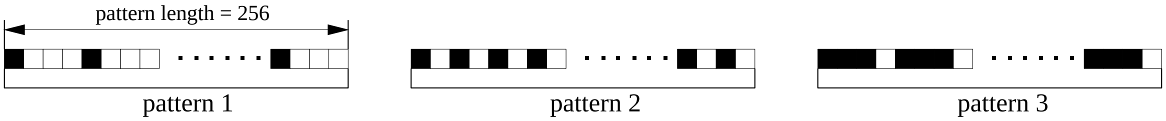

Figure 6: 3 patterns associated with the first row of $[\tau_{ij}]$ in Figure 5.

be:

$$i = x \bmod M, \quad j = y \bmod N.$$

If $I_{xy} > \tau_{ij}$, the picture element (PEL) at position (x, y) is turned on. Figure 5 illustrates an ordered dithering process in the area of uniform intensity $I_{xy} = 6.4$ for $M = N = 4$. In a bilevel system, the ordered dithering provides $MN + 1$ intensity levels while reducing spatial resolution by $1/M$ and $1/N$ on each axis.

When the image is to be produced on a device that can faithfully display binary PELs, the preferred choice of ordered dither is one that generates *dispersed* rather than clustered dots. Dispersed-dot dither arrays yield high frequency fidelity and illusions of gray regions better than do clustered-dot arrays of the same resolution and period [19], as shown in Figure 3-(a,b). An optimality criterion for the dispersed-dot ordered dither was proposed by Bayer [22] and used to generate dither patterns that do not introduce much low frequency noise into a displayed image [21]. Bayer's algorithm measures undesirable low frequency textures in terms of a Fourier anaysis of the dither patterns at different intensity levels. When the dither pattern in the area of uniform intensity has components at several different wave-lengths, the component with the longest finite wave-length should contribute most to the undesirable low frequency textures in the uniform patch. By using the longest wave-length as a measure of the simulated halftone quality, a necessary and sufficient rule has been derived by Bayer [22] for the optimum order, i.e., dither pattern, of adding on-PELs to the lattice. Judice *et al.* [23] derived a recurrence relation to compute dither array $D^{(n)}$ from $D^{(n/2)}$ which obeys Bayer's rule:

$$D^{(n)} = \begin{bmatrix} 4D^{(n/2)} & 4D^{(n/2)} + 2U^{(n/2)} \\ 4D^{(n/2)} + 3U^{(n/2)} & 4D^{(n/2)} + U^{(n/2)} \end{bmatrix}, \tag{1}$$

$$\text{where} \quad U^{(n)} = \begin{bmatrix} 1 & 1 & \cdots & 1 \\ 1 & 1 & \cdots & 1 \\ . & . & . & . \\ 1 & 1 & \cdots & 1 \end{bmatrix} \quad \text{and} \quad D^{(2)} = \begin{bmatrix} 0 & 2 \\ 3 & 1 \end{bmatrix}.$$

For instance, a 4×4 dither array shown in Figure 5 corresponds to Bayer's $D^{(4)}$ in Eq. (1).

2.2 Layerwise Dithering

In 3D Printing, there are two schemes to minimize the amount of data which must be stored and downloaded. The first is to specify not a complete location-mapped instruction of the part, but rather a series of charging voltage changes, or *transitions*, occurring at certain locations such as feature edges. The second is the use of *pattern memories*, which like downloadable fonts in a laser printer make it easy to print *repetitive* patterns of droplet placement for surface texturing and local control of material compositions. The use of pattern memories is especially efficient in many applications of LCC with 3D Printing, where compositions vary smoothly in most regions of the part. Currently, the 3D Printing device can load up to *eight* different patterns *per nozzle per pass* along the high speed scan direction. For an M by N ordered dither array, a nozzle is responsible for one of those

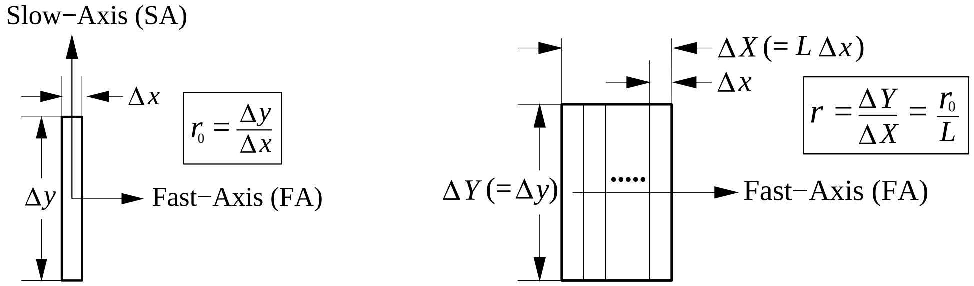

(a) 3D Printer's PEL

(b) An equivalent PEL

Figure 7: PEL geometry

M rows per pass, which implies that it is enough to assign $N+1$ patterns to each nozzle per pass, while the associated dithering provides the full $MN+1$ different intensity levels. Furthermores, as *all on-PELs* and *all off-PELs* can be defined by transition instructions, *only* $N-1$ *different patterns* are actually required per nozzle per pass. For example, in order to describe the patterns of the first row of a 4×4 dither array shown in Figure 5, we need only 3 patterns except all-on/all-off as shown in Figure 6. In this way, the use of rectangular *ordered* dither facilitates the control of the number of dither patterns represented within the limit of 3D Printer's pattern memories.

In most applications of 3D Printing, having the material distributed as uniformly as possible is desirable, and we are relying on diffusion to make the composition locally uniform. While the fusion can smooth out high frequency variations of composition, it will be more difficult to smooth out low frequency composition variations in a reasonable amount of time. The desire to reduce low frequency content makes Bayer's algorithm a sensible point of departure for 3D Printing, even though the motivation is quite different from that of graphics industry where low frequency content degrades the visual appearance of the displayed images. Bayer's original formulation is based on the assumption that PELs are in the same isotropic shape, which is reasonable for the traditional hardcopy printing where PEL shapes can be defined as square or regular hexagon. However, in case of 3D Printing device, PEL shape is a rectangle with *high aspect ratio* r_0 up to 20 – see Figure 7-(a), where Fast-Axis (FA) denotes high speed scan direction and Slow-Axis (SA) denotes the direction perpendicular to FA on 3D Printer's raster grid [7].

3D Printing device, like conventional laser printers and film recorders, cannot very faithfully reproduce isolated on-PELs. Due to the print-head speed and the rates at which droplets are formed, there is a distance between two adjacent droplets along FA on the powder bed. If the frequency of droplet generation is f and the print-head moves at speed v, the distance d between two adjacent droplets will be v/f. However, as the droplet frequency and the print-head speed usually fluctuate around the pre-defined values, it is difficult to predict the precise droplet placement inside d. On the other hand, the upper limit of hardware resolution equals PEL width Δx. To make sure that there is always a droplet available when needed, we let L PELs in d-wide region have an *identical* value, where *minimum run-length* L is defined as

$$L = \frac{d}{\Delta x} = \frac{v}{f \Delta x}. \tag{2}$$

For instance, if droplet frequency $f = 40\text{kHz}$, print-head speed $v = 1.2\text{m/s}$ and PEL width $\Delta x = 10\mu\text{m}$, then the required minimum run-length $L = 3$.

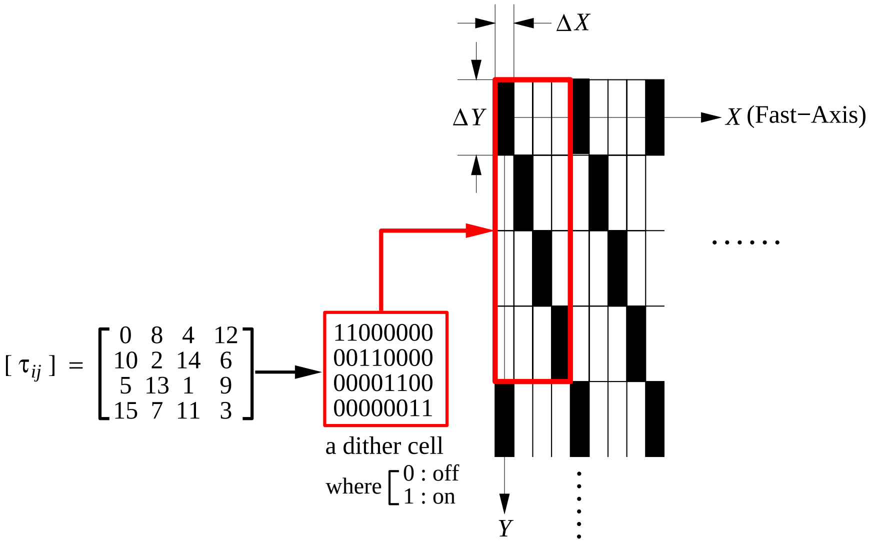

Figure 8: Area of uniform intensity ($M = N = 4$, $L = 2$, $r_0 = 8$, $r = r_0/L = 4$, intensity level $= 5$)

The Bayer's algorithm will be adapted by taking the above two requirements, i.e., the high aspect ratio r_0 of PEL geometry and the minimum run-length L, into account. First, to meet the minimum run-length requirement, let us define an *equivalent* PEL as a PEL with its width ΔX and height ΔY being $L\Delta x$ and Δy, respectively, and thus with aspect ratio[2] $r = \Delta Y/\Delta X = r_0/L$, as shown in Figure 7-(b). The equivalent PEL at its coordinates (i, j) corresponds to L PELs at the 3D Printer's raster coordinates (iL, j), $(iL + 1, j)$, $\cdots$, $(iL + L - 1, j)$, where $0 \leq i < n/L$, $0 \leq j < m$, and m, n are the number of rows and colums of 3D Printer's raster grid. This implies that intensifying an equivalent PEL forces the associated L PELs along the Fast-Axis to be turned on. Now the construction of $M \times N$ dither array which obeys Bayer's rule can be defined as

Given:

1. M, N: number of rows and columns of a dither array,
2. L: pre-defined minimum run-length,
3. r_0: aspect ratio ($= \Delta x/\Delta y$) of PELs on 3D Printer's raster grid,

Compute: dither array $[\tau_{ij}]$, where $0 \leq i < M$ and $0 \leq j < N$, which satisfies Bayer's criterion for the lattice of equivalent PELs of aspect ratio $r = r_0/L$.

Suppose that an area of uniform intensity is represented by repeating both vertically and horizontally an M by N sub-array of rectangular elements of width ΔX, height ΔY. For example, for $M = N = 4$, $L = 2$, and $r_0 = 8$, if dither array $[\tau_{ij}]$ is determined as in Figure 8, an area of uniform intensity (level 5) must be described by repeating both vertically and horizontally a *dither cell* composed of 4-on and 12-off equivalent PELs (i.e., 8-on and 24-off PELs on the original raster grid), as illustrated in Figure 8. That is, let $I(X, Y)$ be the intensity value, 0 or 1, at $(X, Y) = (k\Delta X, l\Delta Y)$ where $0 \leq k < N$ and $0 \leq l < M$, then

$$I(X + N\Delta X,\ Y) = I(X,\ Y + M\Delta Y) = I(X, Y), \tag{3}$$

i.e.,

$$I(\,(k + N)\Delta X,\ l\Delta Y) = I(k\Delta X,\ (l + M)\Delta Y) = I(k\Delta X, l\Delta Y). \tag{3$'$}$$

---

[2] In the current configuration of 3D Printing device, we notice the aspect ratio r reaches about 6.

Hence the basic sub-array $I(k\Delta X, l\Delta Y)$ can be represented by two-dimensional discrete Fourier transform [24, 22]:

$$I(X,Y) = I(k\Delta X, l\Delta Y) := \sum_{u=-N/2+1}^{N/2} \sum_{v=-M/2+1}^{M/2} J(\frac{u}{N\Delta X}, \frac{v}{M\Delta Y}) e^{-i2\pi(\frac{uk}{N}+\frac{vl}{M})} \tag{4}$$

where,

$$J(\frac{u}{N\Delta X}, \frac{v}{M\Delta Y}) := \frac{1}{MN} \sum_{k=0}^{N-1} \sum_{l=0}^{M-1} I(k\Delta X, l\Delta Y) e^{i2\pi(\frac{uk}{N}+\frac{vl}{M})}. \tag{5}$$

The real part of each term in Eq. (4) is a sinusoidal plane wave component with *amplitude* A_{uv}, given by

$$A_{uv} = \sqrt{J(\frac{u}{N\Delta X}, \frac{v}{M\Delta Y})\ J(\frac{-u}{N\Delta X}, \frac{-v}{M\Delta Y})}, \tag{6}$$

and a *wave length* λ_{uv} measured at right angles in the wave front

$$\lambda_{uv} = \frac{L_X L_Y}{\sqrt{(L_Y u)^2 + (L_X v)^2}}, \tag{7}$$

in XY-plane, where L_X and L_Y are the width and height of a dither cell, respectively, i.e.,

$$L_X = N\Delta X, \qquad L_Y = M\Delta Y. \tag{8}$$

An *index of texture* Λ in an area of uniform intensity is defined by the longest finite wave-length of the non-zero sinusoidal components of dither patterns [22], i.e.,

$$\Lambda := \max_{u,v}\{\lambda_{uv} | A_{uv} \neq 0,\ \lambda_{uv} < \infty\}. \tag{9}$$

Construction of an $M \times N$ dither array is thus accomplished by choosing a *sequence* of MN positions within M by N lattice that *minimizes* Λ for *each* level of intensity. At an intensity level, if different choices of positions give an identical $\min(\Lambda)$, we choose the one whose next largest λ_{uv} is less, and so on in a similar way in case the next largest λ_{uv} is also identical.

Table 1 shows the resulting $2^m \times 2^m$ dither arrays according to the change of array size and aspect ratio r of the equivalent PEL. It is obvious that the results for $r = 1$ are identical to those from Eq. (1). Figures 9 and 10 show the corresponding gray scale ramps for $m = 3$ and $r = 4, 6$, respectively and their comparison with Bayer's original thresholding from Eq. (1). Table 2 and Figure 11 also show the resulting $2^2 \times 2^3$ dither arrays for $r = 1, 2, 4, 6$, and comparison of gray scale ramps for $r = 6$, respectively. In Figure 11-(a), conventional odd period pattern with D_a in Table 2 is used. Improvement with regard to the criterion of minimizing Λ which yields higher degree of dispersion of dots can be observed in those Figures 9, 10 and 11. Ulichney [19] provided a detailed investigation of *compensated* dithering arrays on rectangular grids of any aspect ratio by extrapolating his hexagonal grid solution. Despite its satisfactory performance, a difficulty in applying the compensated dithering to 3D Printing lies in the constraint of the limited pattern memories – currently affording eight patterns per nozzle per pass – of 3D Printing device described earlier in this section.

Initially our dithering algorithm was meant for LCC with *two* materials, where given an $M \times N$ dither array $[\tau_{ij}^{(1)}]$ for the first material constructed by our criteria, the other $M \times N$ dither array

	r			
m	1	2	4	6
1	$D^{(2)}$	$D^{(2)}$	$D^{(2)}$	$D^{(2)}$
2	$D_a^{(4)}$	$D_b^{(4)}$	$D_c^{(4)}$	$D_c^{(4)}$
3	$D_a^{(8)}$	$D_b^{(8)}$	$D_c^{(8)}$	$D_d^{(8)}$

$$D^{(2)} = \begin{bmatrix} 0 & 2 \\ 3 & 1 \end{bmatrix}, \quad D_a^{(4)} = \begin{bmatrix} 0 & 8 & 2 & 10 \\ 12 & 4 & 14 & 6 \\ 3 & 11 & 1 & 9 \\ 15 & 7 & 13 & 5 \end{bmatrix}, \quad D_b^{(4)} = \begin{bmatrix} 0 & 8 & 4 & 12 \\ 6 & 14 & 2 & 10 \\ 1 & 9 & 5 & 13 \\ 7 & 15 & 3 & 11 \end{bmatrix}, \quad D_c^{(4)} = \begin{bmatrix} 0 & 8 & 4 & 12 \\ 10 & 2 & 14 & 6 \\ 5 & 13 & 1 & 9 \\ 15 & 7 & 11 & 3 \end{bmatrix},$$

$$D_a^{(8)} = \begin{bmatrix} 0 & 32 & 8 & 40 & 2 & 34 & 10 & 42 \\ 48 & 16 & 56 & 24 & 50 & 18 & 58 & 26 \\ 12 & 44 & 4 & 36 & 14 & 46 & 6 & 38 \\ 60 & 28 & 52 & 20 & 62 & 30 & 54 & 22 \\ 3 & 35 & 11 & 43 & 1 & 33 & 9 & 41 \\ 51 & 19 & 59 & 27 & 49 & 17 & 57 & 25 \\ 15 & 47 & 7 & 39 & 13 & 45 & 5 & 37 \\ 63 & 31 & 55 & 23 & 61 & 29 & 53 & 21 \end{bmatrix}, \quad D_b^{(8)} = \begin{bmatrix} 0 & 32 & 16 & 48 & 4 & 36 & 20 & 52 \\ 24 & 56 & 8 & 40 & 28 & 60 & 12 & 44 \\ 6 & 38 & 22 & 54 & 2 & 34 & 18 & 50 \\ 30 & 62 & 14 & 46 & 26 & 58 & 10 & 42 \\ 1 & 33 & 17 & 49 & 5 & 37 & 21 & 53 \\ 25 & 57 & 9 & 41 & 29 & 61 & 13 & 45 \\ 7 & 39 & 23 & 55 & 3 & 35 & 19 & 51 \\ 31 & 63 & 15 & 47 & 27 & 59 & 11 & 43 \end{bmatrix},$$

$$D_c^{(8)} = \begin{bmatrix} 0 & 32 & 16 & 48 & 8 & 40 & 24 & 56 \\ 12 & 44 & 28 & 60 & 4 & 36 & 20 & 52 \\ 2 & 34 & 18 & 50 & 10 & 42 & 26 & 58 \\ 14 & 46 & 30 & 62 & 6 & 38 & 22 & 54 \\ 1 & 33 & 17 & 49 & 9 & 41 & 25 & 57 \\ 13 & 45 & 29 & 61 & 5 & 37 & 21 & 53 \\ 3 & 35 & 19 & 51 & 11 & 43 & 27 & 59 \\ 15 & 47 & 31 & 63 & 7 & 39 & 23 & 55 \end{bmatrix}, \quad D_d^{(8)} = \begin{bmatrix} 0 & 32 & 16 & 48 & 4 & 36 & 20 & 52 \\ 8 & 40 & 24 & 56 & 12 & 44 & 28 & 60 \\ 18 & 50 & 2 & 34 & 22 & 54 & 6 & 38 \\ 26 & 58 & 10 & 42 & 30 & 62 & 14 & 46 \\ 5 & 37 & 21 & 53 & 1 & 33 & 17 & 49 \\ 13 & 45 & 29 & 61 & 9 & 41 & 25 & 57 \\ 23 & 55 & 7 & 39 & 19 & 51 & 3 & 35 \\ 31 & 63 & 15 & 47 & 27 & 59 & 11 & 43 \end{bmatrix}.$$

Table 1: $2^m \times 2^m$ dither arrays for different aspect ratio r of PELs

r			
1	2	4	6
D_a	D_b	D_c	D_d

$$D_a = \begin{bmatrix} 0 & 16 & 4 & 20 & 1 & 17 & 5 & 21 \\ 24 & 8 & 28 & 12 & 25 & 9 & 29 & 13 \\ 6 & 22 & 2 & 18 & 7 & 23 & 3 & 19 \\ 30 & 14 & 26 & 10 & 31 & 15 & 27 & 11 \end{bmatrix}, \quad D_b = \begin{bmatrix} 0 & 16 & 8 & 24 & 2 & 18 & 10 & 26 \\ 12 & 28 & 4 & 20 & 14 & 30 & 6 & 22 \\ 3 & 19 & 11 & 27 & 1 & 17 & 9 & 25 \\ 15 & 31 & 7 & 23 & 13 & 29 & 5 & 21 \end{bmatrix},$$

$$D_c = \begin{bmatrix} 0 & 16 & 8 & 24 & 4 & 20 & 12 & 28 \\ 6 & 22 & 14 & 30 & 2 & 18 & 10 & 26 \\ 1 & 17 & 9 & 25 & 5 & 21 & 13 & 29 \\ 7 & 23 & 15 & 31 & 3 & 19 & 11 & 27 \end{bmatrix}, \quad D_d = \begin{bmatrix} 0 & 16 & 8 & 24 & 4 & 20 & 12 & 28 \\ 10 & 26 & 2 & 18 & 14 & 30 & 6 & 22 \\ 5 & 21 & 13 & 29 & 1 & 17 & 9 & 25 \\ 15 & 31 & 7 & 23 & 11 & 27 & 3 & 19 \end{bmatrix}.$$

Table 2: $2^2 \times 2^3$ dither arrays for different aspect ratio r of PELs

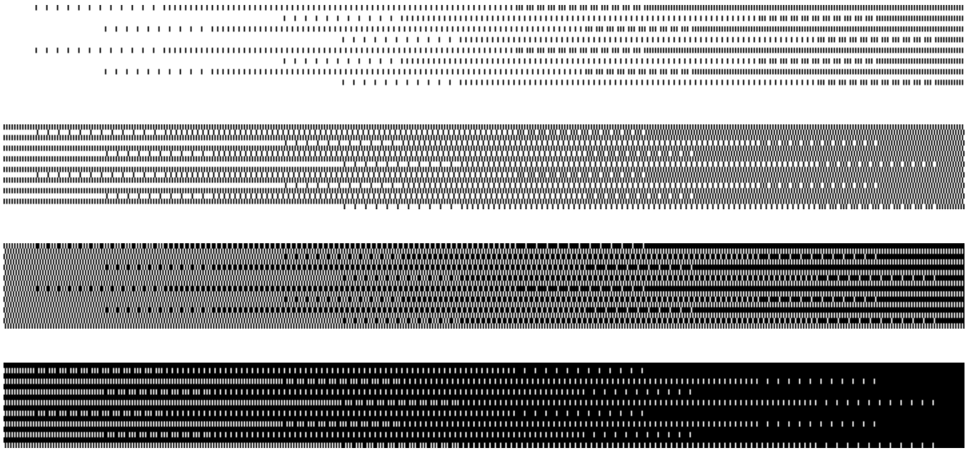

(a) Bayer's original thresholding

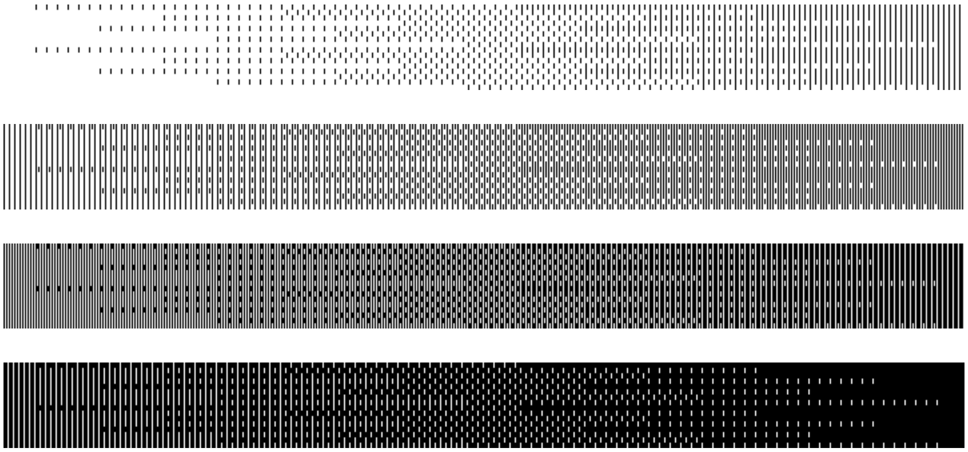

(b) proposed (adapted) thresholding

Figure 9: Comparison: gray scale ramps ($m = 3$, $r = 4$)

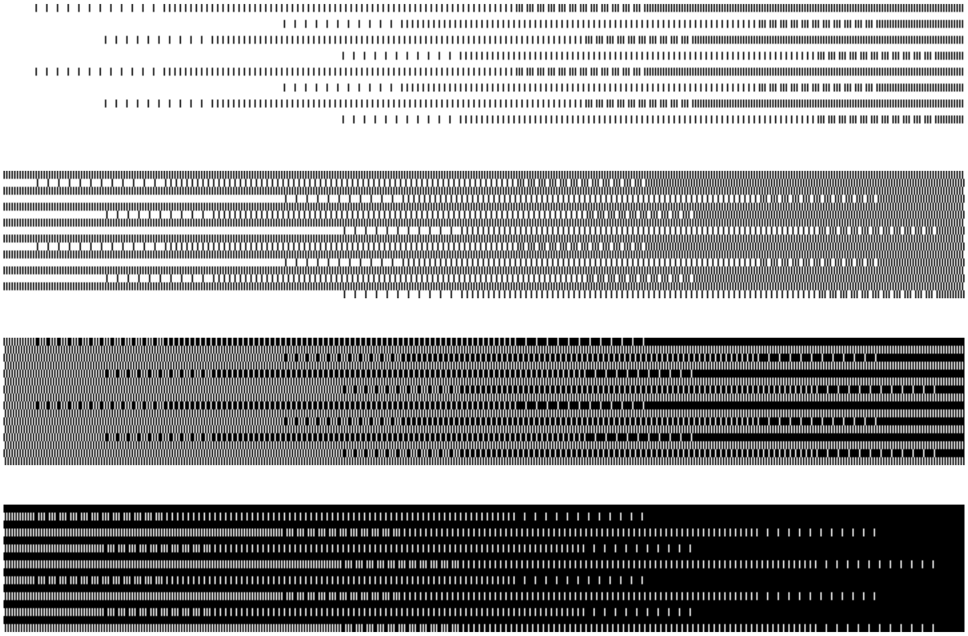

(a) Bayer’s original thresholding

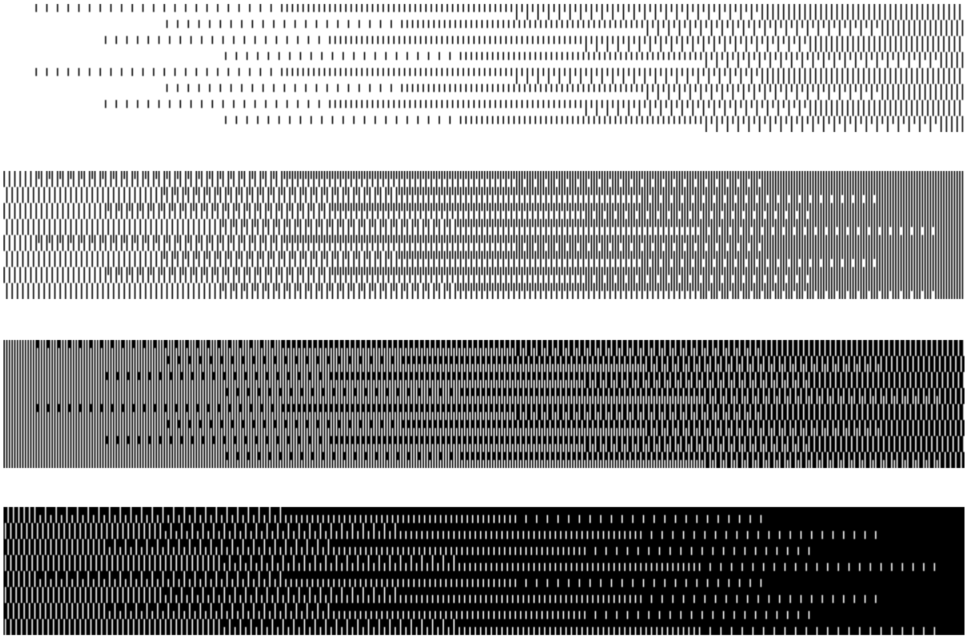

(b) proposed (adapted) thresholding

Figure 10: Comparison: gray scale ramps ($m = 3$, $r = 6$)

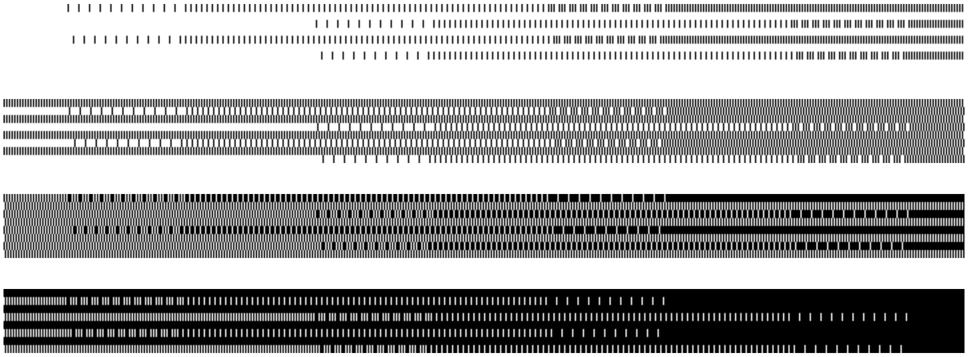

(a) Bayer's original thresholding

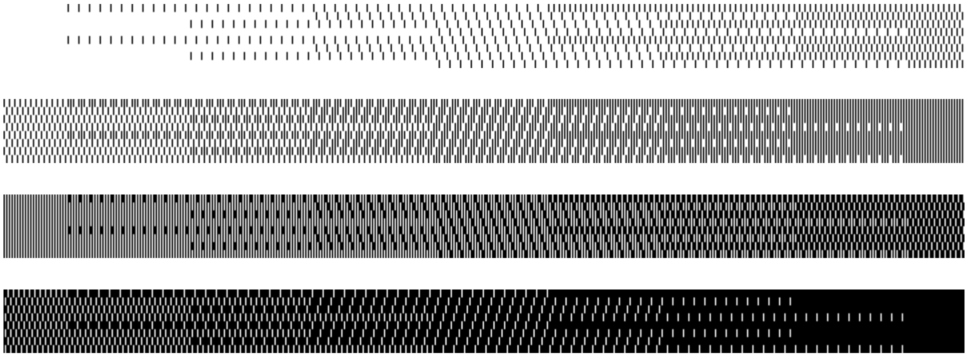

(b) proposed (adapted) thresholding

Figure 11: Comparison: gray scale ramps ($2^2 \times 2^3$ dither arrays, $r = 6$)

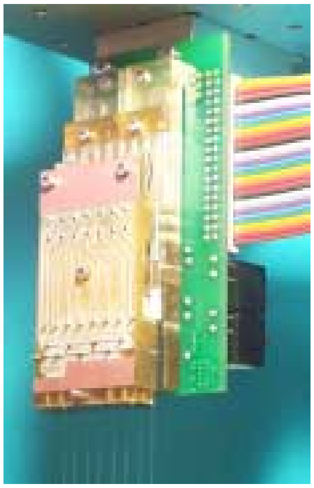

Figure 12: A scalable multiple nozzle print-head

$[\tau^{(2)}_{ij}]$ for the second material can be constructed by the following simple relation:

$$\tau^{(1)}_{ij} + \tau^{(2)}_{ij} = MN - 1, \tag{10}$$

i.e., $[\tau^{(2)}_{ij}]$ retains the identical degree of dispersion to that of $[\tau^{(1)}_{ij}]$ while disallowing overwritten droplets of different materials for $\rho^{(1)}_{xy} + \rho^{(2)}_{xy} \not> 1$, which is preferable in 3D Printing applications, where $\rho^{(1)}_{xy}$ and $\rho^{(2)}_{xy}$ denote normalized intensity or volume fraction of the first and second material at position (x, y) on a layer. Although we have not yet practiced printing more than two materials, a scalable multiple nozzle print-head [7] (see also Figure 12) developed by MIT is configured with two banks of four jets, which has provisions for LCC with (up to) four materials. At present, given a base dither array $[\tau_{ij}]$ constructed by the proposed algorithm, dithering for LCC with $N_m (\geq 2)$ materials is constructed by the constraint that dither array $[\tau^{(k)}_{ij}]$ $(k = 1, 2, \cdots, N_m)$ for each material retains the identical degree of dispersion to that of $[\tau_{ij}]$ while minimizing the number of overwritten droplets of different materials for $\sum_{k=1}^{N_m} \rho_k = 1$ by properly mirroring and shifting the base dither array $[\tau_{ij}]$, where ρ_k denotes normalized uniform intensity or volume fraction of the k-th material over the dither cell. We notice that this approach is reduced to Eq. (10) for $N_m = 2$. Here, by mirroring a $2^m \times 2^n$ dither array $[\tau_{ij}]$, we mean

$$\tau^{(k)}_{ij} = \tau_{i,2^n-j-1} \quad \text{or} \quad \tau^{(k)}_{ij} = \tau_{2^m-i-1,j} \tag{11}$$

Shifting $[\tau_{ij}]$ by l along j-axis results in

$$\tau^{(k)}_{ij} = \begin{cases} \tau_{i,j-l} & \text{if } j - l \geq 0, \\ \tau_{i,j-l+2^n} & \text{if } j - l < 0, \end{cases} \tag{12}$$

where $0 < l < 2^n$. Similarly, shifting a dither array along i-axis can be defined. For example, 4×4 dither arrays $D_{(k)}$ for $N_m = 4$ and $r = 6$, using $D^{(4)}_c$ in Table 1 as a base dither array, result in

$$D_{(1)} = \begin{bmatrix} 5 & 13 & 1 & 9 \\ 10 & 2 & 14 & 6 \\ 0 & 8 & 4 & 12 \\ 15 & 7 & 11 & 3 \end{bmatrix}, D_{(2)} = \begin{bmatrix} 2 & 10 & 6 & 14 \\ 13 & 5 & 9 & 1 \\ 7 & 15 & 3 & 11 \\ 8 & 0 & 12 & 4 \end{bmatrix}, D_{(3)} = \begin{bmatrix} 8 & 0 & 12 & 4 \\ 2 & 10 & 6 & 14 \\ 13 & 5 & 9 & 1 \\ 7 & 15 & 3 & 11 \end{bmatrix}, D_{(4)} = \begin{bmatrix} 11 & 7 & 15 & 3 \\ 4 & 8 & 0 & 12 \\ 14 & 2 & 10 & 6 \\ 1 & 13 & 5 & 9 \end{bmatrix}. \tag{13}$$

As an alternative way, we can utilize a color digital halftoning technique [25] which extends Bayer's approach using multi-cluster halftone cells. For example, Cook's [25] spatial relationships for our 4×4 halftone cell represented by 4-cluster case is as follows for $N_m = 4$ and $r = 6$ using $D^{(4)}_c$ in Table 1,

$$\begin{bmatrix} M^{(1)}_0 & M^{(3)}_0 & M^{(2)}_0 & M^{(4)}_0 \\ M^{(3)}_2 & M^{(1)}_2 & M^{(4)}_2 & M^{(2)}_2 \\ M^{(2)}_1 & M^{(4)}_1 & M^{(1)}_1 & M^{(3)}_1 \\ M^{(4)}_3 & M^{(2)}_3 & M^{(3)}_3 & M^{(1)}_3 \end{bmatrix},$$

where $M^{(k)}_i$ denotes k-th material's cluster i, and the corresponding dither array $D_{(k)}$ for each material results in

$$D_{(1)} = \begin{bmatrix} 0 & 8 & 4 & 12 \\ 10 & 2 & 14 & 6 \\ 5 & 13 & 1 & 9 \\ 15 & 7 & 11 & 3 \end{bmatrix}, D_{(2)} = \begin{bmatrix} 4 & 12 & 0 & 8 \\ 14 & 6 & 10 & 2 \\ 1 & 9 & 5 & 13 \\ 11 & 3 & 15 & 7 \end{bmatrix}, D_{(3)} = \begin{bmatrix} 12 & 0 & 8 & 4 \\ 2 & 14 & 6 & 10 \\ 9 & 5 & 13 & 1 \\ 7 & 11 & 3 & 15 \end{bmatrix}, D_{(4)} = \begin{bmatrix} 8 & 4 & 12 & 0 \\ 6 & 10 & 2 & 14 \\ 13 & 1 & 9 & 5 \\ 3 & 15 & 7 & 11 \end{bmatrix}. \tag{14}$$

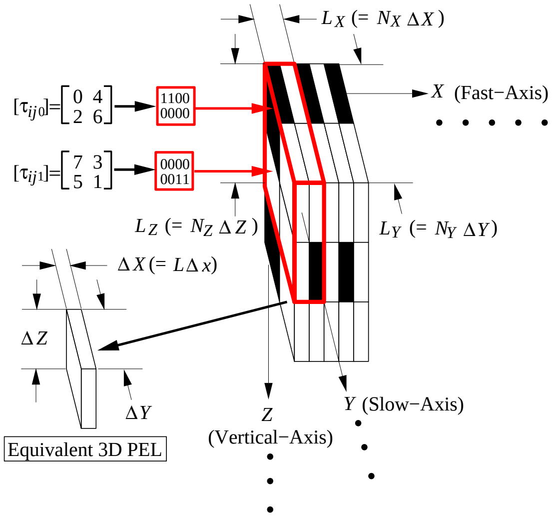

Figure 13: A volume of uniform intensity (level 2, $N_X = N_Y = N_Z = 2$, $L = 2$)

We notice each $D_{(k)}$ in both Eq. (13) and Eq. (14) retains the identical degree of dispersion to that of $D_c^{(4)}$ in Table 1. For areas of uniform composition, where the normalized intensities ρ_k for all four materials are less than 1/4, none of the clusters will overlap. At $\rho_1 = \rho_2 = \rho_3 = \rho_4 = 1/4$, the clusters will tessellate the patch. Similarly, $\rho_1 = \rho_3 = 1/2$ with $\rho_2 = \rho_4 = 0$ will tessellate the patch as will $\rho_2 = \rho_4 = 1/2$ with $\rho_1 = \rho_3 = 0$.

2.3 Extension to Volume Dithering

Due to the three-dimensionality of the 3D Printing process, it will be necessary to create *volume* dithering patterns in order for successive layers not to be printed with the same pattern in the region of fairly uniform composition. We note that replicating layers of the same two-dimensional dither pattern will create vertical streaks of the same material. Two-dimensional dithering algorithm described so far can be readily extended to three-dimensional case with a criterion that the minimization of the longest finite wavelength of the nonzero sinusoidal components that describe the dot pattern of a *volume* of uniform intensity, i.e.,

Given:

1. N_X, N_Y, N_Z: size of a 3D dither array in fast, slow, and vertical axis, respectively,
2. L: pre-defined minimum run-length along the fast axis,
3. Δx, Δy, Δz : dimension of a 3D PEL in fast, slow, and vertical axis, respectively,

Compute: dither array $[\tau_{ijk}]$, where $0 \leq i < N_Y$, $0 \leq j < N_X$, $0 \leq k < N_Z$, which satisfies Bayer's criterion for the lattice of equivalent PELs of dimension $\Delta X = L\Delta x$, $\Delta Y = \Delta y$, $\Delta Z = \Delta z$ in each axis – e.g., see Figure 13 for dithering a volume of uniform intensity (level 2) using a $2 \times 2 \times 2$ dither array $[\tau_{ijk}]$ with $L = 2$.

Then, Eqs. (3) – (8) can be re-derived as follows for 3D dithering:

$$I(X + N_X\Delta X,\ Y,\ Z) = I(X,\ Y + N_Y\Delta Y,\ Z) = I(X,\ Y,\ Z + N_Z\Delta Z) = I(X, Y, Z), \tag{15}$$

i.e.,

$$I(\,(l+N_X)\Delta X,\ m\Delta Y,\ n\Delta Z) = I(l\Delta X,\ (m+N_Y)\Delta Y,\ n\Delta Z) = \\ I(l\Delta X,\ m\Delta Y,\ (n+N_Z)\Delta Z) = I(l\Delta X, m\Delta Y, n\Delta Z). \tag{15'}$$

The basic subarray can be specified by all combinations of such l, m, n and hence,

$$I(X,Y,Z) = I(l\Delta X, m\Delta Y, n\Delta Z) := \\ \sum_{u=-N_X/2+1}^{N_X/2} \sum_{v=-N_Y/2+1}^{N_Y/2} \sum_{w=-N_Z/2+1}^{N_Z/2} J(\frac{u}{N_X\Delta X}, \frac{v}{N_Y\Delta Y}, \frac{w}{N_Z\Delta Z})\, e^{-i2\pi(\frac{ul}{N_X}+\frac{vm}{N_Y}+\frac{wn}{N_Z})}, \tag{16}$$

where,

$$J(\frac{u}{N_X\Delta X}, \frac{v}{N_Y\Delta Y}, \frac{w}{N_Z\Delta Z}) := \frac{1}{N_X N_Y N_Z} \sum_{l=0}^{N_X-1} \sum_{m=0}^{N_Y-1} \sum_{n=0}^{N_Z-1} I(l\Delta X, m\Delta Y, n\Delta Z)\, e^{i2\pi(\frac{ul}{N_X}+\frac{vm}{N_Y}+\frac{wn}{N_Z})}. \tag{17}$$

The real part of each term in Eq. (16) is a sinusoidal wave with an amplitude A_{uvw}, given by

$$A_{uvw} = \sqrt{J(\frac{u}{N_X\Delta X}, \frac{v}{N_Y\Delta Y}, \frac{w}{N_Z\Delta Z})\ J(\frac{-u}{N_X\Delta X}, \frac{-v}{N_Y\Delta Y}, \frac{-w}{N_Z\Delta Z})} \tag{18}$$

and a wave length λ_{uvw} is given by

$$\lambda_{uvw} = \frac{L_X L_Y L_Z}{\sqrt{(L_Y L_Z u)^2 + (L_Z L_X v)^2 + (L_X L_Y w)^2}}, \tag{19}$$

where $L_X = N_X \Delta X$, $L_Y = N_Y \Delta Y$, $L_Z = N_Z \Delta Z$, i.e., the length of each edge of a 3D dither cell.

An *index of texture* Λ in a volume of uniform intensity is defined by

$$\Lambda := \max_{u,v,w}\{\lambda_{uvw} | A_{uvw} \neq 0, \lambda_{uvw} < \infty\}. \tag{20}$$

Thus, construction of a 3D dither array. which provides $N_X N_Y N_Z + 1$ intensity levels, consists of choosing a sequence of $N_X N_Y N_Z$ positions within N_X by N_Y by N_Z lattice that minimize Λ for each level of intensity.

Table 3 shows the resulting $2^m \times 2^m \times 2^m$ $(m = 1, 2)$ dither arrays according to the change of aspect ratio $r = \Delta Y/\Delta X = \Delta Z/\Delta X$ of the equivalent PEL, where we set $\Delta Y = \Delta Z$ for simplicity and due to the fact that the order of magnitude of ΔY is usually that of ΔZ (i.e., layer thickness) in 3D Printing[3]. Furthermore, Table 4 shows the resulting $2^2 \times 2^3 \times 2$ dither arrays for $r = 1, 2, 4, 6$. Figure 14 shows the corresponding gray scale ramps along X (i.e, fast scan direction) for $r = 6$, where $[\tau_{ij0}]$ ($[\tau_{ij1}]$) is used for layer number being even (odd), respectively.

3 Implementation

The LCC information pathway with 3D Printing begins with a designer interacting with a standard CAD system to define the shape of the object, see Figure 15-(A). The solid model thus created is then exported from the CAD system in a standard exchange format such as STEP [29] or IGES [30]. In the course of our work, we implemented an LCC modeler [12, 13, 31, 28, 32, 33] based on tetrahedral mesh data structure. Once the geometry of the model is fully defined, it is loaded into a finite-element mesh generator via a neutral format, and meshed into a set of tetrahedra. This process is referred to as *pre-processing* in Figure 15-(A). The composition of a part is established by specifying the composition values at the vertices of each tetrahedron and interpolating between them. As an exemplar of a design tool, we developed a method to specify a

---

[3] Of course, the algorithm itself is general in terms of the ratio among ΔX, ΔY, and ΔZ.

	r			
m	1	2	4	6
1	$[\tau^{(2)}_{ijk}]$	$[\tau^{(2)}_{ijk}]$	$[\tau^{(2)}_{ijk}]$	$[\tau^{(2)}_{ijk}]$
2	$[\tau^{(4)}_{ijk}]_a$	$[\tau^{(4)}_{ijk}]_b$	$[\tau^{(4)}_{ijk}]_c$	$[\tau^{(4)}_{ijk}]_c$

$$[\tau^{(2)}_{ij0}] = \begin{bmatrix} 0 & 2 \\ 4 & 6 \end{bmatrix}, \quad [\tau^{(2)}_{ij1}] = \begin{bmatrix} 7 & 5 \\ 3 & 1 \end{bmatrix},$$

$$[\tau^{(4)}_{ij0}]_a = \begin{bmatrix} 0 & 14 & 22 & 32 \\ 10 & 50 & 40 & 18 \\ 52 & 44 & 4 & 24 \\ 58 & 30 & 38 & 46 \end{bmatrix}, \quad [\tau^{(4)}_{ij1}]_a = \begin{bmatrix} 56 & 8 & 16 & 54 \\ 12 & 2 & 48 & 6 \\ 28 & 36 & 60 & 42 \\ 26 & 62 & 34 & 20 \end{bmatrix}, \quad [\tau^{(4)}_{ij2}]_a = \begin{bmatrix} 5 & 25 & 53 & 45 \\ 39 & 47 & 59 & 31 \\ 23 & 33 & 1 & 15 \\ 41 & 19 & 11 & 51 \end{bmatrix}, \quad [\tau^{(4)}_{ij3}]_a = \begin{bmatrix} 61 & 43 & 29 & 37 \\ 35 & 21 & 27 & 63 \\ 17 & 55 & 57 & 9 \\ 49 & 7 & 13 & 3 \end{bmatrix},$$

$$[\tau^{(4)}_{ij0}]_b = \begin{bmatrix} 0 & 40 & 16 & 56 \\ 52 & 28 & 36 & 12 \\ 2 & 42 & 18 & 58 \\ 54 & 30 & 38 & 14 \end{bmatrix}, \quad [\tau^{(4)}_{ij1}]_b = \begin{bmatrix} 32 & 8 & 48 & 24 \\ 20 & 60 & 4 & 44 \\ 34 & 10 & 50 & 26 \\ 22 & 62 & 6 & 46 \end{bmatrix}, \quad [\tau^{(4)}_{ij2}]_b = \begin{bmatrix} 3 & 43 & 19 & 59 \\ 55 & 31 & 39 & 15 \\ 1 & 41 & 17 & 57 \\ 53 & 29 & 37 & 13 \end{bmatrix}, \quad [\tau^{(4)}_{ij3}]_b = \begin{bmatrix} 35 & 11 & 51 & 27 \\ 23 & 63 & 7 & 47 \\ 33 & 9 & 49 & 25 \\ 21 & 61 & 5 & 45 \end{bmatrix},$$

$$[\tau^{(4)}_{ij0}]_c = \begin{bmatrix} 0 & 56 & 16 & 30 \\ 60 & 26 & 4 & 48 \\ 18 & 2 & 28 & 58 \\ 24 & 6 & 50 & 62 \end{bmatrix}, \quad [\tau^{(4)}_{ij1}]_c = \begin{bmatrix} 54 & 32 & 12 & 44 \\ 36 & 8 & 40 & 22 \\ 52 & 46 & 34 & 14 \\ 10 & 38 & 42 & 20 \end{bmatrix}, \quad [\tau^{(4)}_{ij2}]_c = \begin{bmatrix} 29 & 59 & 19 & 3 \\ 51 & 63 & 25 & 7 \\ 17 & 31 & 1 & 57 \\ 5 & 49 & 61 & 27 \end{bmatrix}, \quad [\tau^{(4)}_{ij3}]_c = \begin{bmatrix} 35 & 15 & 53 & 47 \\ 43 & 21 & 11 & 39 \\ 13 & 45 & 55 & 33 \\ 41 & 23 & 37 & 9 \end{bmatrix}.$$

Table 3: $2^m \times 2^m \times 2^m$ dither arrays for different aspect ratio r of PELs

r			
1	2	4	6
$[\tau_{ijk}]_a$	$[\tau_{ijk}]_b$	$[\tau_{ijk}]_c$	$[\tau_{ijk}]_d$

$$[\tau_{ij0}]_a = \begin{bmatrix} 0 & 16 & 4 & 20 & 1 & 17 & 5 & 21 \\ 56 & 40 & 60 & 44 & 57 & 41 & 61 & 45 \\ 6 & 22 & 2 & 18 & 7 & 23 & 3 & 19 \\ 62 & 46 & 58 & 42 & 63 & 47 & 59 & 43 \end{bmatrix}, \quad [\tau_{ij1}]_a = \begin{bmatrix} 32 & 48 & 36 & 52 & 33 & 49 & 37 & 53 \\ 24 & 8 & 28 & 12 & 25 & 9 & 29 & 13 \\ 38 & 54 & 34 & 50 & 39 & 55 & 35 & 51 \\ 30 & 14 & 26 & 10 & 31 & 15 & 27 & 11 \end{bmatrix},$$

$$[\tau_{ij0}]_b = \begin{bmatrix} 0 & 40 & 16 & 56 & 2 & 42 & 18 & 58 \\ 52 & 28 & 36 & 12 & 54 & 30 & 38 & 14 \\ 3 & 43 & 19 & 59 & 1 & 41 & 17 & 57 \\ 55 & 31 & 39 & 15 & 53 & 29 & 37 & 13 \end{bmatrix}, \quad [\tau_{ij1}]_b = \begin{bmatrix} 32 & 8 & 48 & 24 & 34 & 10 & 50 & 26 \\ 20 & 60 & 4 & 44 & 22 & 62 & 6 & 46 \\ 35 & 11 & 51 & 27 & 33 & 9 & 49 & 25 \\ 23 & 63 & 7 & 47 & 21 & 61 & 5 & 45 \end{bmatrix},$$

$$[\tau_{ij0}]_c = \begin{bmatrix} 0 & 32 & 20 & 52 & 8 & 40 & 28 & 60 \\ 26 & 58 & 14 & 46 & 18 & 50 & 6 & 38 \\ 1 & 33 & 21 & 53 & 9 & 41 & 29 & 61 \\ 27 & 59 & 15 & 47 & 19 & 51 & 7 & 39 \end{bmatrix}, \quad [\tau_{ij1}]_c = \begin{bmatrix} 16 & 48 & 4 & 36 & 24 & 56 & 12 & 44 \\ 10 & 42 & 30 & 62 & 2 & 34 & 22 & 54 \\ 17 & 49 & 5 & 37 & 25 & 57 & 13 & 45 \\ 11 & 43 & 31 & 63 & 3 & 35 & 23 & 55 \end{bmatrix},$$

$$[\tau_{ij0}]_d = \begin{bmatrix} 0 & 40 & 16 & 56 & 4 & 44 & 20 & 60 \\ 50 & 26 & 34 & 10 & 54 & 30 & 38 & 14 \\ 5 & 45 & 21 & 61 & 1 & 41 & 17 & 57 \\ 55 & 31 & 39 & 15 & 51 & 27 & 35 & 11 \end{bmatrix}, \quad [\tau_{ij1}]_d = \begin{bmatrix} 32 & 8 & 48 & 24 & 36 & 12 & 52 & 28 \\ 18 & 58 & 2 & 42 & 22 & 62 & 6 & 46 \\ 37 & 13 & 53 & 29 & 33 & 9 & 49 & 25 \\ 23 & 63 & 7 & 47 & 19 & 59 & 3 & 43 \end{bmatrix}.$$

Table 4: $2^2 \times 2^3 \times 2$ dither arrays for different aspect ratio r of PELs

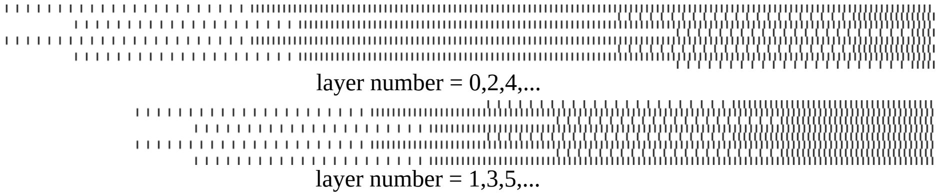

(a) $0 \leq \rho \leq 1/4$

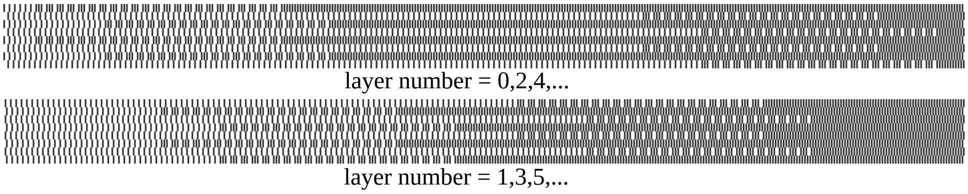

(b) $1/4 \leq \rho \leq 1/2$

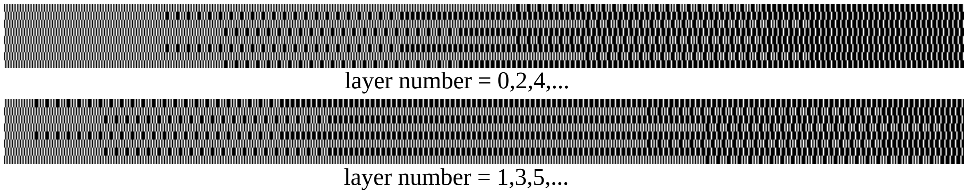

(c) $1/2 \leq \rho \leq 3/4$

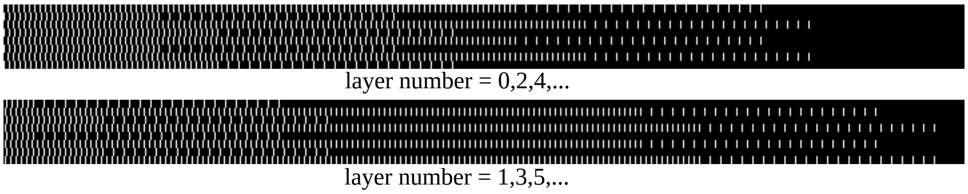

(d) $3/4 \leq \rho \leq 1$

Figure 14: Gray scale ramps using $2^2 \times 2^3 \times 2$ dither array for $r = 6$, where ρ denotes the normalized intensity level or volume fraction

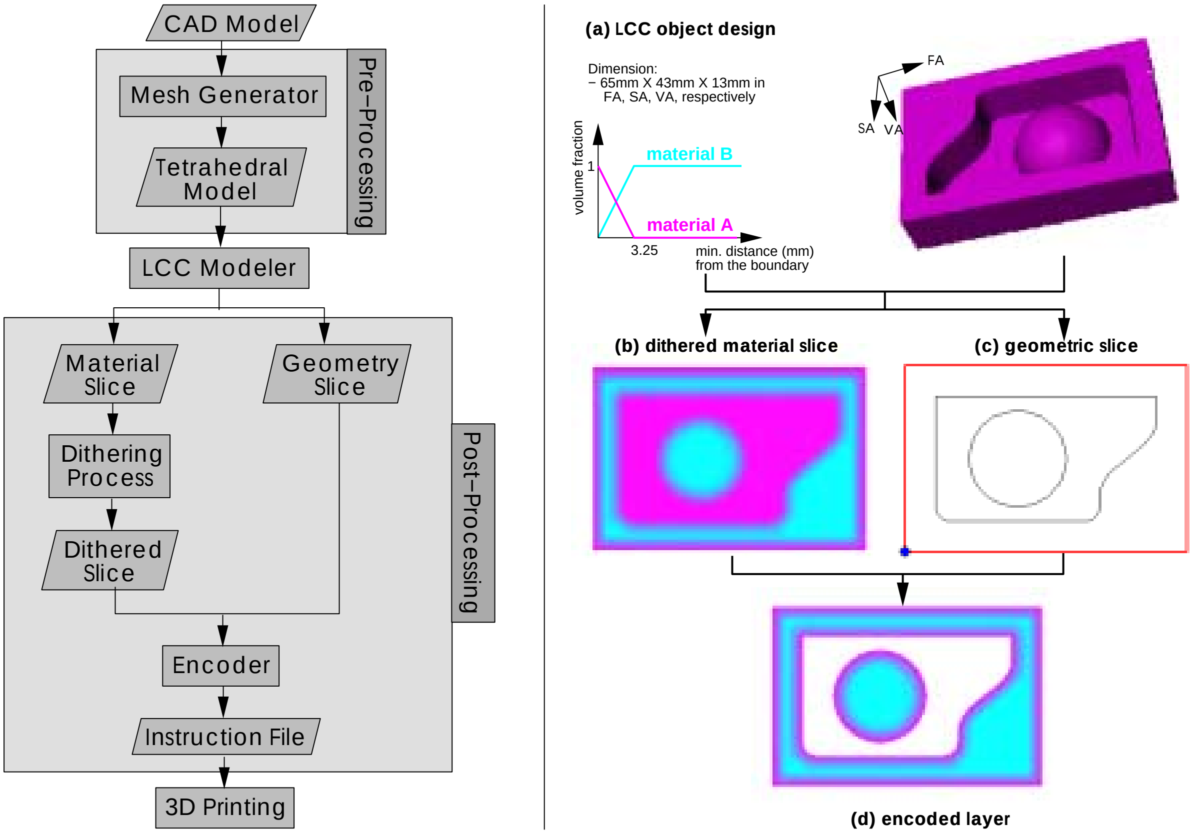

(A) Information pathway

(B) Demonstration of information pathway

Figure 15: Illustration of information flow for LCC with 3D Printing

composition profile as a function of minimum distance to the object's boundary and applied this profile to an entire object [31]. *Post-processing* then converts the designed LCC model into machine instructions for the 3D Printing device. Post-processing takes place on a layer-by-layer basis along two parallel paths: (1) the accurate definition of the surface (Geometry Slice); and (2) rendering the composition of the body (Material Slice). The continuous-tone material composition is rendered into printable discrete information using the proposed dithering algorithms. The boundary and composition information is recombined to produce the drop-by-drop instructions that are loaded onto the 3D Printing machine. We note that our dithering algorithm is not subject to a specific LCC modeling method but can be applied to various kinds of LCC modelers for Solid Freeform Fabrication (SFF) e.g., voxel-based, finite-element mesh-based, and generalized modeling methods such as those based on extended radial-edge or cell-tuple-graph data structures [34].

We have implemented the proposed dithering algorithm with a mold example shown in Figure 15-(B-a). Physical dimension of the bounding box of the part is $6.5cm \times 4.3cm \times 1.3cm$ in fast, slow, and vertical axis, respectively. We set the width of an equivalent PEL $\Delta X = 30\mu m$ and its aspect ratio $r = 6$. The composition for the object is designed as a function of minimum distance from the object's boundary to place hard phases in a designed composition profile near the boundary surface by locally controlling the volume fraction of two materials. In this example, the composition grades linearly over the region within $3.25\,mm$ of the object's boundary with the condition that the sum of volume fraction of two materials is everywhere one, creating a skin of designed composition. Figures 16, 17 and Figures 18, 19 show enlarged views of a dithered layer (about half-way up the part) for each material using 4×8 2D and $4 \times 8 \times 2$ 3D thresholding with aspect ratio of PEL $r = 6$ – see also the corresponding dither array D_d in Table 2 and $[\tau_{ij0}]_d$ in Table 4 for material A, and Eq. (10) for material B in two-material composition.

As observed in Figures 16 and 18, the ordered dither inevitably produces blurred/coarse boundary or surface finish. Special attention needs to be given to reconciling conflicts which occur at the boundary where the designer's intent in both composition and surface finish must be recognized. Edge enhancement has been investigated in digital halftoning research such as constrained average [26] and dot diffusion [27] algorithms. In 3D Printing, the issue of boundary reconciliation is taken care of in the *encoding* stage [28, 13] which is a part of post-processing. Although the detailed encoding scheme is beyond the scope of this article, we briefly describe major techniques associated with surface finish in 3D Printing.

3D printing uses continuous-jet printing with a capability of *proportional deflection* [7]. In proportionally deflected printing, droplets can be steered to any position within the maximum deflection range in the slow-axis direction. Figure 20-(a) shows the pattern that would be created using binary control of a continuous-jet printhead, where the raster pattern results in a step-wise approximation to the desired contour of the part. The use of proportional deflection shown in Figure 20-(b) offers significant potential to improve the quality of the printed parts with no compromise in production rate. To achieve an accurate composition/geometry near the boundary, an algorithm is required which identifies the necessary boundary droplets to be printed and the amount of their proportional deflections. Especially, the algorithm should guarantee the concentration C_b of the sum of all *binder* materials satisfies a required amount C_τ at the boundary. Such required amount will vary from system to system, however, would typically be between 10% – 50% of full saturation. Figure 20-(c) would be the resulting surface finish if $C_b < C_\tau$. At present [13], C_τ is forced to be 100% and the amount of proportional deflection is computed from the geometric boundary information – as illustrated in Figure 15-(B-b,c,d), for technical simplicity, dithering assigns the composition at the geometric boundary to the region outside the boundary, which is trimmed away by the geometric slice.

4 Conclusions

Among the Solid Freeform Fabrication (SFF) technologies, Three-Dimensional Printing (3D Printing) is particularly well-suited to the fabrication of parts with Local Composition Control (LCC). This article has developed a dithering algorithm which provides an intermediate representation scheme to convert an idealized computer model with functionally graded materals (FGM) into its machine instructions for LCC with 3D Printing.

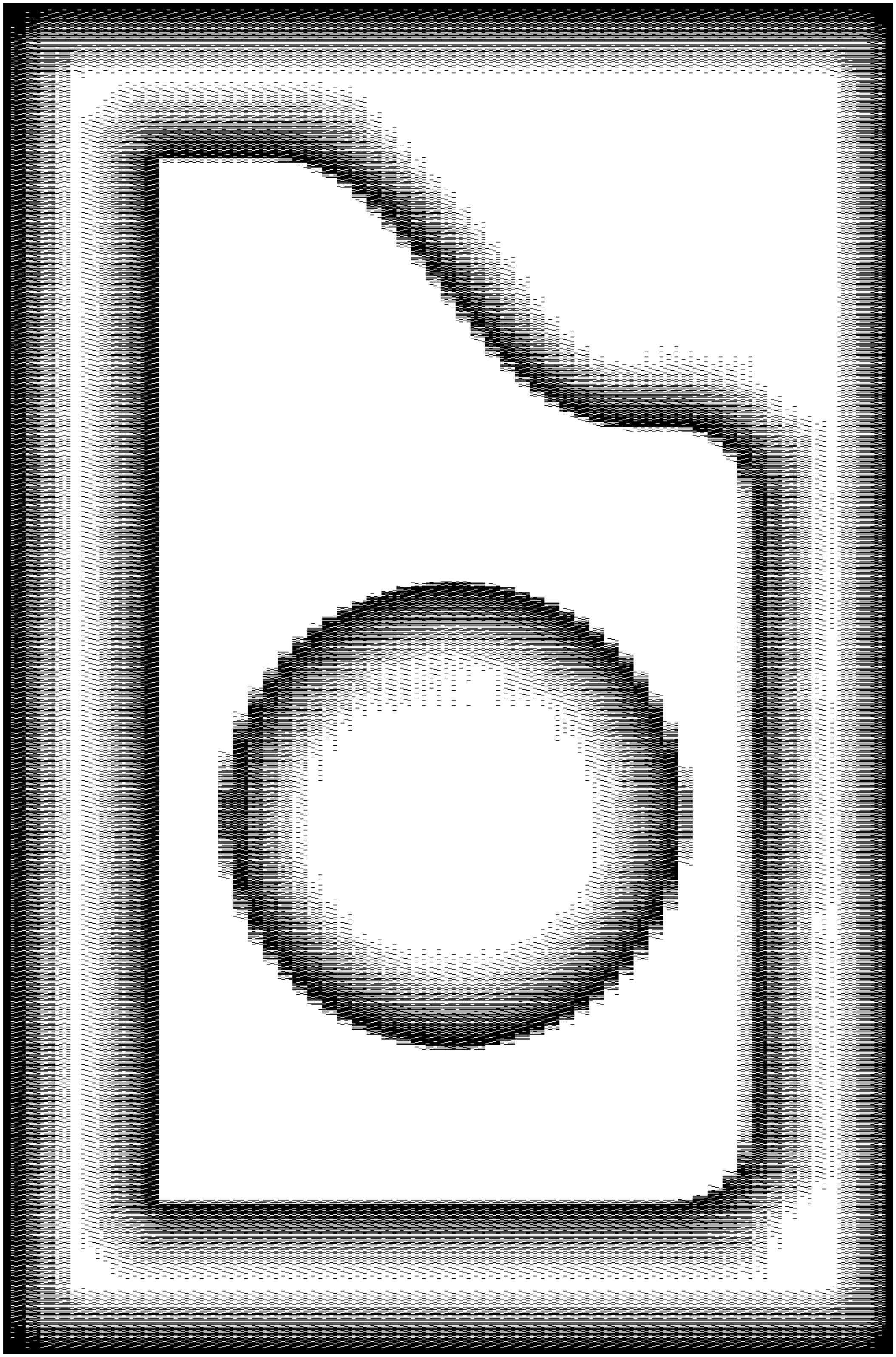

Figure 16: A dithered layer for material A using 4 × 8 2D dither array with $r = 6$

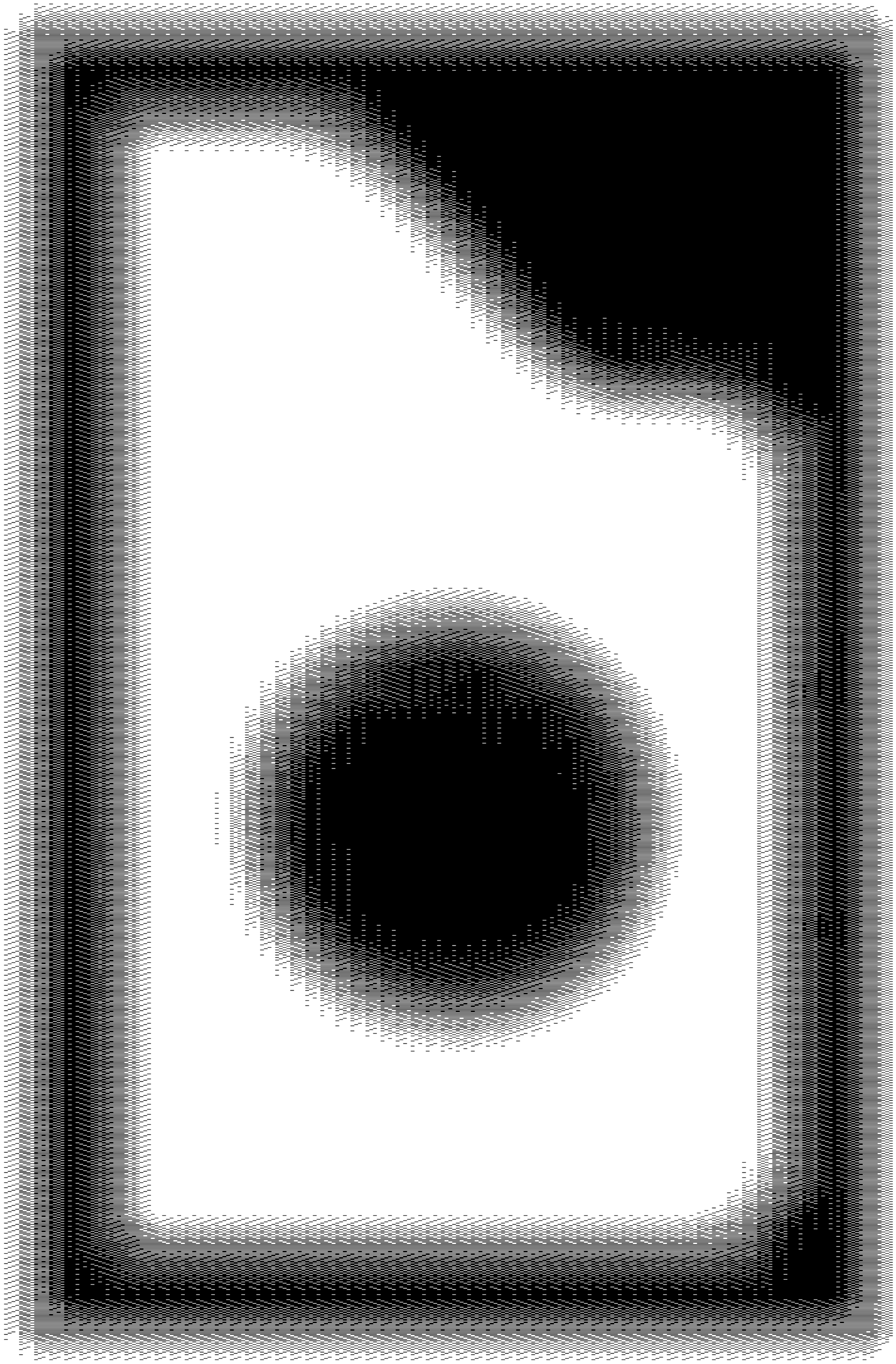

Figure 17: A dithered layer for material B using 4×8 2D dither array with $r = 6$

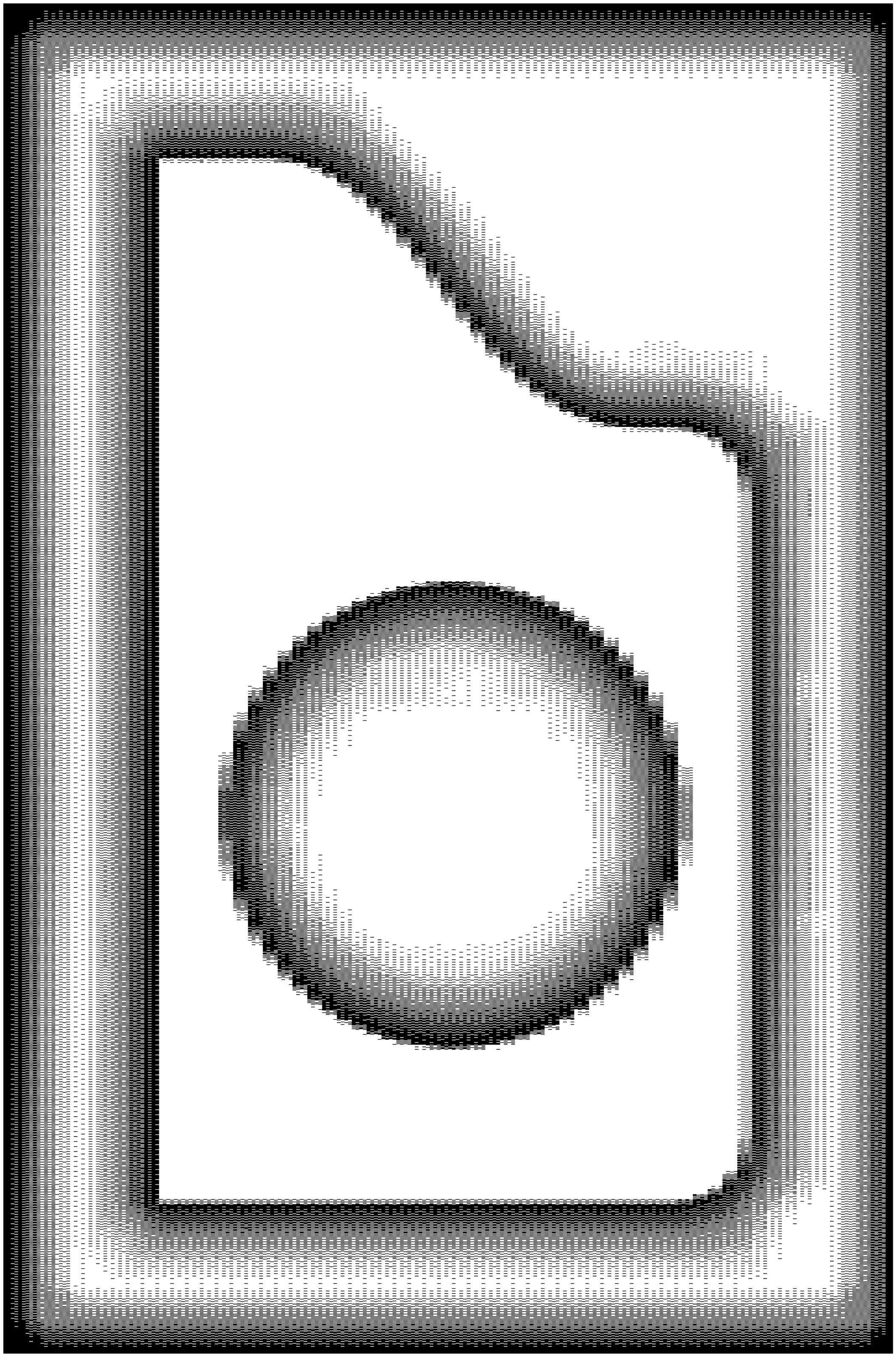

Figure 18: A dithered layer for material A using 4 × 8 × 2 3D dither array with $r = 6$ (for even number layers)

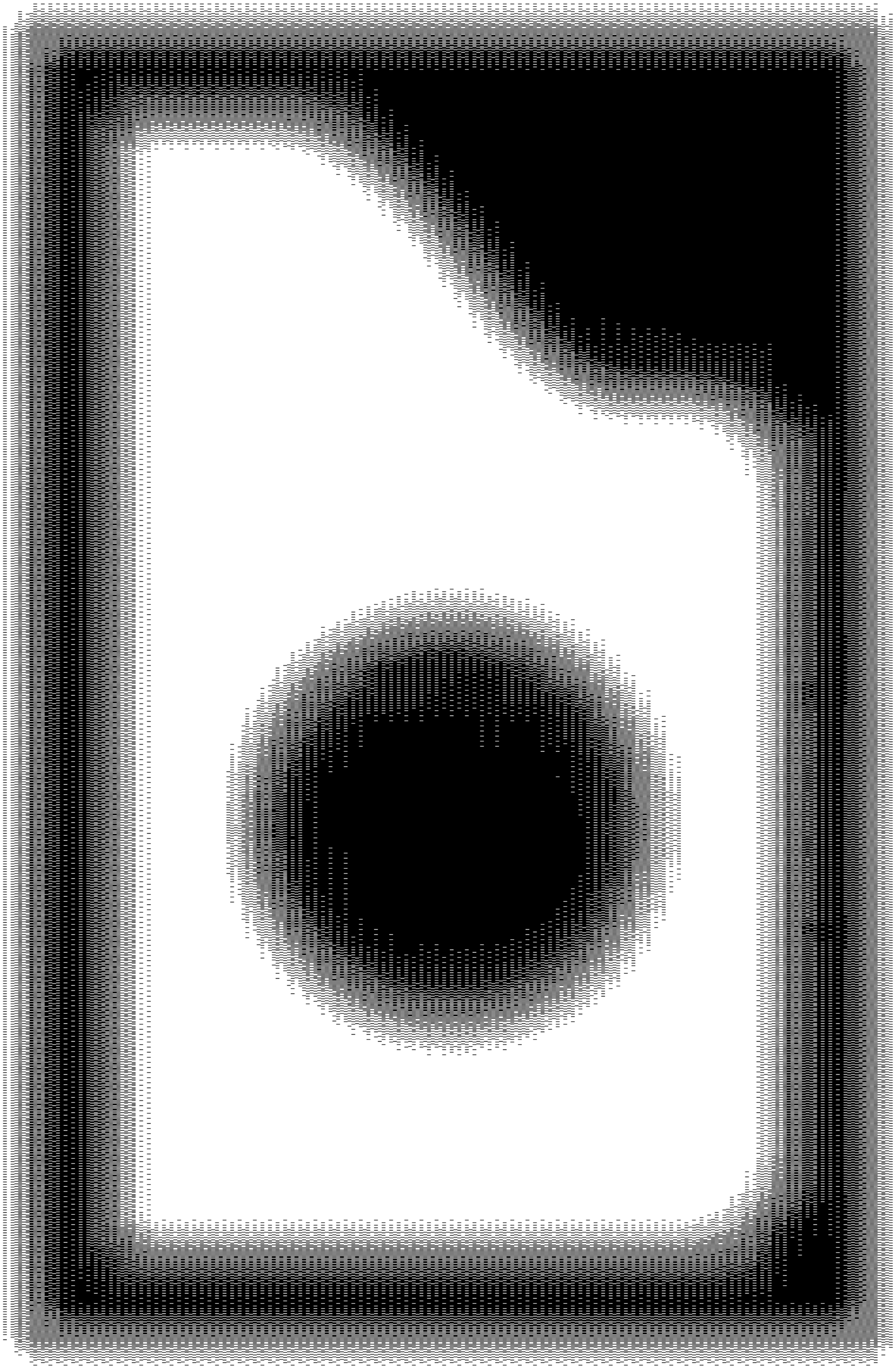

Figure 19: A dithered layer for material B using 4 × 8 × 2 3D dither array with $r = 6$ (for even number layers)

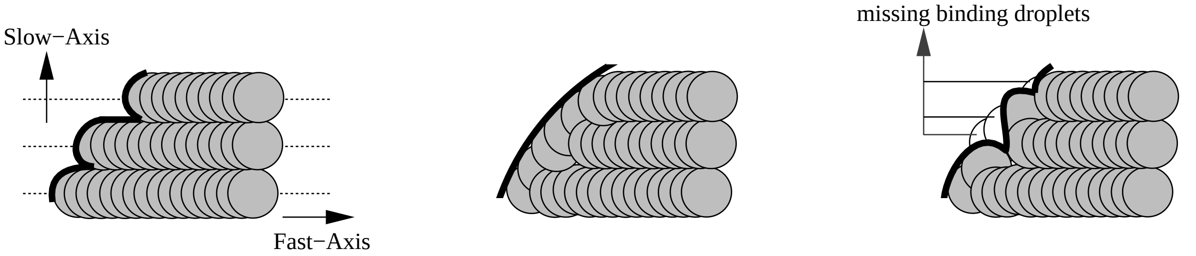

(a) without proportional deflection (b) proportionally deflected printing (c) insufficient binding droplets

Figure 20: Proportional deflection and surface finish

The proposed algorithm uses a *rectangular ordered* dither which facilitates the control of the number of dither patterns represented within the limit of 3D Printer's *pattern memories.* The algorithm also uses a *dispersed-dot* ordered dither based on Bayer's criterion to avoid low frequency textures of composition but is adaped to address the *anisotropic* PEL geometry and *uncertainties* in droplet placement. Considering the three-dimensionality of the 3D Printing process, Bayer's criterion is further extended to create *volumewise* dither patterns, which also keep successive layers from being printed with the same patterns in the region of fairly uniform compositions. Our dithering algorithm is not associated with a specific LCC modeling/fabrication method but can be applied to various types of LCC modelers/point-wise fabrication processes in SFF fields.

To achieve an accurate composition/geometry near the boundary, a *general* encoding scheme needs to be further developed which guarantees sufficient binding at the surface to satisfy the geometric design intent with the minimum possible deviation from the composition design intent.

Acknowledgment

Funding for this work was obtained in part from NSF and ONR under grants DMI-9617750, DMI-0100194 and N00014-00-1-0169.

References

[1] D. L. Bourell, R. H. Crawford, H. L. Marcus, J. J. Beaman, and J. W. Barlow. Selective laser sintering of metals, In *Proceedings of the 1994 ASME Winter Annual Meeting*, pp. 519–528, Chicago, IL, November 6–11, 1994.

[2] C. Chi. Process insight about LOM systems, In D. L. Bourell *et al.*, editor, *Solid Freeform Fabrication Symposium*, pp. 515–522, Austin, TX, August 1996.

[3] P. F. Jacobs. *Rapid Prototyping and Manufacturing: Fundamentals of Stereolithography*, Society of Manufacturing Engineers, Dearborn, MI, 1992.

[4] L. E. Weiss, R. Merz, F. B. Prinz, G. Neplotnik, P. Padmanabhan. Shape deposition manufacturing of heterogeneous structures. *SME Journal of Manufacturing Systems*, 16(4):239–248, 1997.

[5] K. J. Jakubenas, J. M. Sanchez, and H. L. Marcus. Multiple material solid free-form fabrication by selective area laser deposition. *Materials and Design*, 19(1/2):11–18, 1998.

[6] E. M. Sachs, E. Wylonis, S. Allen, M. J. Cima, and H. Guo. Production of injection molding tooling with conformal cooling channels using the three dimensional printing process, *Polymer Engineering Science*, 40(5):1232–1247, May 2000.

[7] E. M. Sachs, D. Brancazio, J. Milner, J. Serdy, A. Curodeau, and J. Bredt. High rate, high quality 3D printing through machine design, on-line measurement, and control, *International Journal of Machine Tools and Manufacturing*, to appear.

[8] E. M. Sachs, J. Haggerty, M. J. Cima, and P. Williams. Three-Dimensional Printing Techniques, U.S. Patent No. 5204055, April 20, 1993.

[9] E. M. Sachs, M. J. Cima, P. Williams, D. Brancazio, and J. Cornie. Three dimensional printing: rapid tooling and prototypes directly from a CAD model, *Journal of Engineering for Industry,* 114(4):481-488, November 1992.

[10] E. M. Sachs, M. J. Cima, J. Bredt, and A. Curodeau. CAD-casting: direct fabrication of ceramic shells and cores by three dimensional printing, *Manufacturing Review,* 5(2):118-126, June 1992.

[11] T. R. Jackson, W. Cho, N. M. Patrikalakis, and E. M. Sachs. Memory analysis of solid model representations for heterogeneous objects, to appear in *Journal of Computing and Information Science in Engineering,* ASME.

[12] W. Cho, E. M. Sachs, and N. M. Patrikalakis. Solid Freeform Fabrication with Local Composition Control, Invited paper in *Rapid Prototyping*, Quarterly of the Rapid Prototyping Association of the Society of Manufacturing Engineers. 7(2):1–5, Second Quarter Issue, 2001. Dearborn, MI: SME.

[13] W. Cho, E. M. Sachs, N. M. Patrikalakis, M. J. Cima, T. R. Jackson, H. Liu, J. Serdy, C. C. Stratton, H. Wu, and R. Resnick. Methods for distributed design and fabrication of parts with local composition control, *Proceedings of the 2001 NSF Design and Manufacturing Grantees Conference*, Tampa, FL, USA, January 2001.

[14] S.-M. Park, R. H. Crawford, and J. J. Beaman. Volumetric multi-texturing for functionally gradient material representation, In D. C. Anderson and K. Lee, editors, *Sixth ACM Symposium on Solid Modeling and Applications*, June 6-8, 2001, pp. 216–224. New York, 2001. ACM SIGGRAPH.

[15] V. Kumar, D. Burns, D. Dutta, and C. Hoffmann. A framework for object modeling, *Computer-Aided Design*, 31(9):541–556, August, 1999.

[16] V. Kumar and D. Dutta. An approach to modeling and representation of heterogeneous objects, *Journal of Mechanical Design*, 120:659–667, December 1998.

[17] W. E. Katstra, R. D. Palazzolo, C. W. Rowe, B. Giritlioglu, P. Teung, and M. J. Cima. Oral dosage forms fabricated by Three-Dimensional Printing, *Journal of Controlled Release*, 66(1):1–9, May 2000.

[18] C. W. Rowe, W. E. Katstra, R. D. Palazzolo, B. Giritlioglu, P. Teung, and M. J. Cima. Multimechanism oral dosage forms fabricated by Three-Dimensional Printing, *Journal of Controlled Release*, 66(1):1232–1247, May 2000.

[19] R. Ulichney. *Digital Halftoning*, MIT Press, Cambridge, 1987.

[20] J. C. Stoffel and J. F. Moreland. A survey of electronic techniques for pictorial reproduction, *IEEE Transactions on Communications*, 29:1898–1925, 1981.

[21] J. F. Jarvis, C. N. Judice and W. H. Ninke. A survey of techniques for the display of continuous-tone pictures on bilevel displays, *Computer Graphics and Image Processing*, 5:13–40, 1976.

[22] B. E. Bayer. An optimum method for two-level rendition ofcontinuous-tone pictures, *IEEE International Conference on Communications, Conference Record,* 1:(26-11)–(26-15), 1973.

[23] C. N. Judice, J. F. Jarvis, and W. H. Ninke. Using ordered dither to display continuous tone picture on an AC plasma panel, *Proceedings of the Society for Information Display,* 15(4):161–169, 1974.

[24] S. L. Marple Jr. *Digital Spectral Analysis with Applications,* Prentice Hall, Inc., New Jersey, 1987.

[25] C. C. Cook. Color digital halftoning using multi-cluster halftone dots, eds. R. A. Morris and J. André, *Raster Imaging and Digital Typography II,* 120–127, The Cambridge Series on Electronic Publishing. MIT Press, Cambridge, MA, 1991.

[26] J. F. Jarvis and C. S. Roberts. A new technique for displaying continuous tone images on a bilevel displays, *IEEE Transactions on Communications*, 24:891–898, 1976.

[27] D. Knuth. Digital halftones by dot diffusion, *ACM Transactions on Graphics*, 6(4):245–273, 1981.

[28] H. Wu, E. M. Sachs, N. M. Patrikalakis, D. Brancazio, J. Serdy, T. R. Jackson, W. Cho, H. Liu, M. J. Cima, and R. Resnick. Distributed design and fabrication of parts with local composition control. *Proceedings of the 2000 NSF Design and Manufacturing Grantees Conference*, Vancouver, BC, Canada, January 2000.

[29] American National Standards Institute. *Product Data Exchange Using STEP (PDES) Part 42, Integrated generic resources: geometric and topological representation.* Fairfax, VA, February 1995.

[30] IGES/PDES Organization, U.S. Product Data Association, Fairfax, VA. *Digital Representation for Communication of Product Definition Data, US PRO/IPO-100, Initial Graphics Exchange Specification (IGES) 5.2*, November 1993.

[31] H. Liu, W. Cho, T. R. Jackson, N. M. Patrikalakis, and E. M. Sachs. Algorithms for design and interrogation of functionally gradient material objects, *Proceedings of 2000 ASME DETC/CIE, 26-th ASME Design Automation Conference,* September, 2000, Baltimore, Maryland, USA. p.141 and CDROM, NY:ASME, 2000.

[32] T. R. Jackson, H. Liu, N. M. Patrikalakis, E. M. Sachs, and M. J. Cima. Modeling and designing functionally graded material components for fabrication with local composition control. *Materials and Design*, 20(2/3):63–75, June 1999.

[33] T. R. Jackson, N. M. Patrikalakis, E. M. Sachs, and M. J. Cima. Modeling and designing components with locally controlled composition. In D. L. Bourell et al, editor, *Solid Freeform Fabrication Symposium*, pages 259–266, Austin, Texas, August 10-12 1998. The University of Texas.

[34] T. R. Jackson. *Analysis of Functionally Graded Material Object Representation Methods,* PhD thesis, Massachusetts Institute of Technology, January 2000.